Alfvénic Modes Excited by the Kink Instability in PHASMA

Peiyun Shi,[1, a)] Prabhakar Srivastava,[1] Cuyler Beatty,[1] Regis John,[1] Matthew Lazo,[1] John McKee,[1] Jacob McLaughlin,[1] Michael Moran,[1] Mitchell Paul,[1] Earl E. Scime,[1, b)] Ethan E. Scime,[1] Derek Thompson,[1] and Thomas Steinberger[1]

Department of Physics and Astronomy and Center for KINETIC Plasma Physics, West Virginia University, Morgantown, West Virginia 26506, USA

(Dated: 26 January 2021)

Magnetic flux ropes have been successfully created with plasma guns in the newly commissioned PHAse Space MApping (PHASMA) experiment. The flux ropes exhibit the expected $m = 1$ kink instability. The observed threshold current for the onset of this kink instability is half of the Kruskal-Shafranov current limit, consistent with predictions for the non-line tied boundary condition of PHASMA. The helicity, paramagnetism, and growth rate of the observed magnetic fluctuations are also consistent with kink instability predictions. The observed fluctuation frequency appears to be a superposition of a real frequency due to a Doppler shift of the kink mode arising from plasma flow (~ 2 kHz) and a contribution from a wave mode (~ 5 kHz). The dispersion of the wave mode is consistent with an Alfvén wave. Distinct from most previous laboratory studies of flux ropes, the working gas in PHASMA is argon. Thus, the ion cyclotron frequency in PHASMA is quite low and the frequency of the Alfvénic mode plateaus at ~ 0.5 of the ion gyro frequency with increasing background magnetic field strength.

I. INTRODUCTION

A magnetic flux rope is a current-carrying plasma with an embedded helical magnetic field. The field is comprised of a background axial magnetic field B_z, and an azimuthal magnetic field B_θ, generated by an axial plasma current.[1] When the plasma current exceeds a threshold value, the $m = 1$ kink instability appears. The kink instability arises from the imbalance in magnetic pressure forces between inner bunched and outer spread magnetic field lines during transverse perturbations of flux rope column. *Sakurai*[2] first identified kinked structures on the Sun during remote imaging of solar flare events.[3,4] The kink instability drives a variety of explosive solar phenomena, e.g., corona mass injections and magnetic reconnection.[5,6] Kinked structures are also observed in magnetized jets emanating from astrophysical sources.[7] The kink instability plays important roles in a variety of laboratory plasma devices. In tokamaks, kink instabilities distort the plasma torus, drive sawtooth oscillations, and also drive other instabilities.[8] Kink instabilities also facilitate the conversion of toroidal magnetic flux into poloidal magnetic flux during the formation process of spheromak discharges.[9]

Because of broad interest, a number of laboratory experiments have focused on the study of kink instabilities. A sampling of kink instability experiments in linear devices is listed in Table I. To excite the kink instability, the flux rope plasma current, I_{bias}, should exceed a threshold value, $I_{KS}(r) = \alpha \frac{4\pi^2 r^2 B_z}{\mu_0 L_0}$, where I_{KS} is the Kruskal-Shafranov limit and L_0 is the flux rope length.[10] The coefficient $\alpha = 1$ for line tied (LT) boundary conditions and $\alpha = \frac{1}{2}$ for non line tied (NLT) boundary conditions.[11,12] At a (non) line tied boundary in a linear experiment, the end of the flux rope is (free) fixed to a (resistive) conducting surface. Kink instabilities with LT boundary conditions were investigated in the Resistive Wall Mode (ReMW) and Rotating Wall Machine (RWM) devices at the University of Wisconsin-Madison. Internal kink modes and the stabilizing effects of different vessel walls were identified.[13,14] At Caltech, the growth rate of kink instabilities under LT boundary conditions as well as multiscale cascades arising from the kink instability were investigated.[9,15,16] Kink instabilities with NLT boundary conditions were studied on the Reconnection Scaling eXperiment (RSX) device at Los Alamos National Laboratory[17–19] and Large Plasma Device (LAPD) at the University of California, Los Angeles.[20] In these two very different NLT kink studies, the threshold current was experimentally verified to be one half of I_{KS}. In both NLT studies, the observed frequency of the fluctuations was attributed to a Doppler frequency shift, f_D, of a zero frequency kink mode (in the plasma frame) due to either axial flow, f_{VZ}, or $E \times B$ drift, $f_{E\times B}$.

Here we report the appearance of a wave mode with Alfvénic features in a kinking flux rope in the new PHASMA (PHAse Space MApping) experiment at West Virginia University. In PHASMA, the observed frequency of the fluctuations associated with the kink instability is much larger than any plausible Doppler frequency shift and the characteristics of the differential frequency, $f - f_D$, imply the presence of a distinct wave mode. Because the working gas in PHASMA is argon (to facilitate laser induced fluorescence measurements of ions[22,23]), the observed fluctuation frequency is a significant fraction of the ion gyro frequency f_{ci}. Since the kink instability can be thought of as one part of the spectrum of surface Alfvén waves,[21] coupling between low-frequency plasma modes and the kink instability is not entirely unexpected. Kink instabilities have been observed to provide free energy to excite other wave modes in plasmas. For example, the kink instability was recently found to excite whistler modes in the Caltech jet experiment.[24]

This paper is organized as follows: The PHASMA device, the experimental apparatus used to create flux ropes, and the fluctuation diagnostics are described in Section II. The observed fluctuations are identified as kink instabilities in Sec.

a)Electronic mail: peiyun.shi@mail.wvu.edu
b)Electronic mail: earl.scime@mail.wvu.edu

	PHASMA	RSX[21]	ReWM[13]	RWM[14]	LAPD[20]	CalTech[9]
Axial Boundary	NLT	NLT	LT	LT	NLT	LT
Gas Species	Argon	Hydrogen	Hydrogen	Hydrogen	Helium	Hydrogen
Electron Density n_e ($10^{19}m^{-3}$)	5	0.9	4	25	0.1	10
Electron Temperature T_e (eV)	5	12	2	10	4	12
Magnetic Field B_z (Gauss)	375	120	270	600	660	800
Length L_0(m)	1-1.7	0.92	1.2	1.2	11	0.25
Radius R_0 (cm)	2	2	6	9	2.5	5
Bias Current I_{bias} (A)	500	320	5000	5000	75	10^5
Kink Frequency f (kHz)	5-10	25	25	20	5	>100
Doppler Shift f_D (kHz)	f_{VZ}, 1-3	f_{VZ}, 20-40	$f_{E\times B}$, ~ 25	$f_{E\times B}$, ~ 20	f_{VZ}, ~ 5	$\sim$
f/f_{ci}	0.7	0.1	0.06	0.02	0.02	0.1

TABLE I. List of fundamental plasma parameters regarding kink instabilities on different devices

III, including measurements of the instability threshold in terms of the safety factor $q = \frac{I_{bias}}{I_{KS}} < 2$, the right (left) handed helicity for $B_z \| J_z$ ($B_z \| -J_z$), and the paramagnetic nature of the fluctuations. As noted previously, the frequency of the fluctuations is much larger ($5\times$) than the Doppler frequency shift of a kink due to axial flow as described by *Ryutov*.[12] In Sec. IV, we suggest that a plasma mode with a frequency equal to the differential frequency co-exists with kink instability. The Alfvénic nature of the plasma mode is verified by comparison with expectations for Aflvén wave dispersion. A brief summary of the results is given in Section V.

II. EXPERIMENTAL APPARATUS

A. PHASMA Device

Construction of the new PHASMA plasma experiment at West Virginia University was completed in 2019. PHASMA is designed to study space plasma-relevant phenomena, including particle heating and acceleration at kinetic scales during magnetic reconnection,[25] electromagnetic instabilities driven by ion temperature anisotropy and plasma pressure,[26] ion acceleration in expanding plasmas,[27] and cross-field ion flows near plasma-material interfaces immersed in a magnetized, high-density plasma.[28] A key feature of PHASMA is the availibility of volumetric, non-perturbative, laser diagnostics for ion and electron velocity distribution function measurements with spatial resolution at the kinetic scale ($\sim$ mm for the electron inertial length). State-of-the-art laser induced fluorescence (LIF) schemes are available to measure velocity distribution functions of ions[22,23] and neutrals.[29–31] An incoherent Thomson scattering system[32] provides measurements of the electron velocity distribution function.

As shown in Fig. 1, PHASMA consists of two main sections, a helicon plasma source housed on a vacuum chamber 1.7 m in length and 15 cm in diameter and another vacuum vessel 2.7 m in length and 0.4 m in diameter that contains two plasma gun sources and a movable anode. The total three turbomolecular pumps located at the ends of the system provide a total pumping speed of 3800 L/s that maintain a base pressure of $< 2\times10^{-7}$ Torr. A static axial magnetic field up to 2200 Gauss in the helicon plasma source (375 Gauss for plasma gun) is generated with 22 electromagnet coils. Various magnetic field configurations, uniform, flared, and magnetic mirror are created by varying the relative currents in the coils. The helicon source operates at an antenna frequency of 9-15 MHz and RF power up to 2 kW to create steady-state and pulsed plasmas in argon, helium, and xenon.[23,33,34] The plasma guns form pulsed high-density argon, helium, and hydrogen plasmas with repetition rate of 1 shot per minute. The two plasma sources are fully independent and can operate simultaneously. Use of a background helicon generated plasma during plasma gun discharges provides a pre-ionized, target plasma (for manipulation of the neutral density), introduces flows in the interaction region between the plasma gun discharges, and controls density gradients across the interaction region. In addition, background helicon source plasmas provide both steady-state and high repetition rate (> 1 Hz) target plasmas for testing of laser diagnostics. PHASMA accesses a wide range of magnetized plasma operational regimes, e.g., plasma beta $0.001 \sim 1$ and Lundquist number $1 \sim 100$, by independently controlling the plasma density.

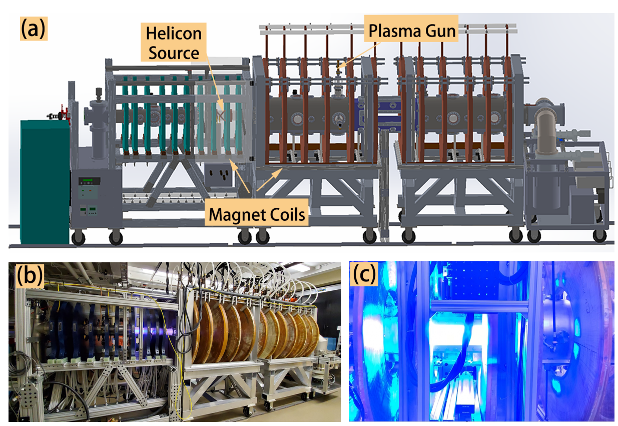

FIG. 1. (a) Solidworks rendering of the PHASMA facility highlighting the helicon source and plasma gun sections. Three turbomolecular pumps maintain a base pressure of $< 2\times10^{-7}$ Torr. Twenty-two solenoid coils are used to generate the background axial magnetic field. (b) Photo of PHASMA with helicon plasma source operating. (c) Photo of an argon plasma gun discharge.

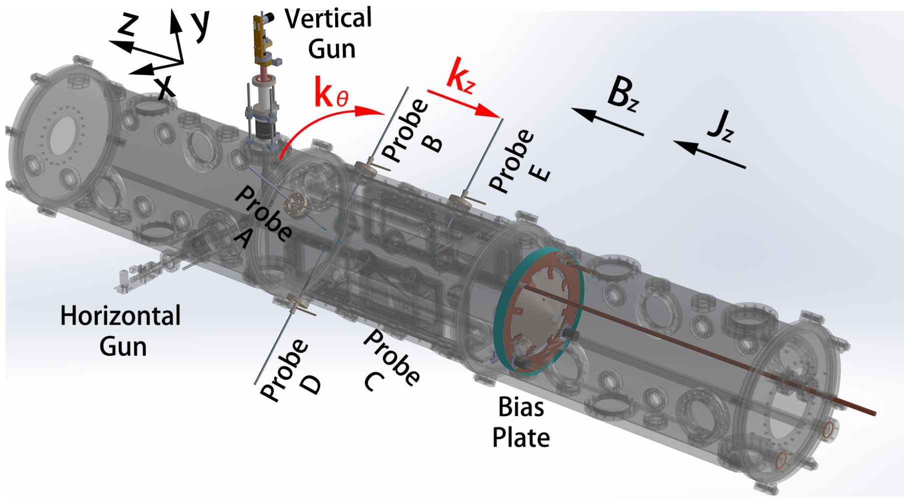

FIG. 2. Schematic of the experimental geometry used for these experiments. The vertical plasma gun and bias plate (anode) were used in these single flux rope studies. Four magnetic probes A, B, C, D are placed equidistant azimuthally while a fifth probe, E, is placed on a different axial plane at the same azimuthal location as probe B. When the background magnetic field, B_z, and the bias current density, J_z, are both along $+\hat{e_z}$, fluctuations propagate $+\hat{e_\theta}$ azimuthally and $-\hat{e_z}$ axially.

B. Flux Rope Formation

Figure 2 shows the experimental geometry for the flux rope experiments. Horizontal and Vertical plasma guns are inserted along the x and y directions at the $z = 0$ plane to launch plasma columns along $-\hat{e_z}$. In these single flux rope studies, only the vertical plasma gun along the y direction is used. The plasma column center is adjustable over 6 cm radially and ± 6 degrees azimuthally. A conical anode (bias plate) is placed at the end of PHASMA to drive axial current along the initial seed plasma columns, thereby forming flux ropes. The conical anode has a diameter of 250 mm and a half angle 60 degrees. The magnetic field penetration time of the anode is approximately 1 μs. The ratio between the Alfvén transit time τ_A and inductive decay time $\tau_{L/R}$, denoted by $\kappa = \frac{\tau_A}{\tau_{L/R}} \gtrsim 10$, confirming that non-line tied boundary condition models are appropriate for these experiments.[12,21] The conical anode is designed to be translated axially from $z = -1.04$ m to -1.73 m.

To characterize the flux rope, four magnetic probes A-D are placed at $z = -0.25$ m, $\theta = \frac{\pi}{4}, \frac{3\pi}{4}, \frac{5\pi}{4}, \frac{7\pi}{4}$ rad and a fifth magnetic probe E is placed at $z = -0.61$ m, $\theta = \frac{3\pi}{4}$. The propagation features of the fluctuations are determined from the phase differences between each probe. All magnetic signals are integrated in real time with active integrator circuits that have a time constant of 10 μs and sampled at 5 MSamples/s. The plasma density and electron temperature are measured with triple Langmuir probes located at $z = 0$ plane.

Figure 3 presents the typical temporal evolution of a single flux rope. Neutral gas injection starts at $t = -38.5$ ms and ends at $t = -1.5$ ms when an arc plasma is generated with a discharge current of approximately 700 A. At $t = 0$ ms, a bias current I_{bias} of 500 A is fired during the plateau of the arc plasma. A flux rope with both axial and azimuthal magnetic fields lasts for more than 10 ms, much longer than the axial Alfvén time $\sim 50\ \mu s$. The azimuthal magnetic field B_θ at $r = 2$ cm is roughly 15 Gauss. Large fluctuations appear before the bias current reaches the peak value and persist for the remainder of the discharge. The plasma density and electron temperature at $r = 0$ cm also increase due to the additional Ohmic heating and ionization when the bias current is triggered.

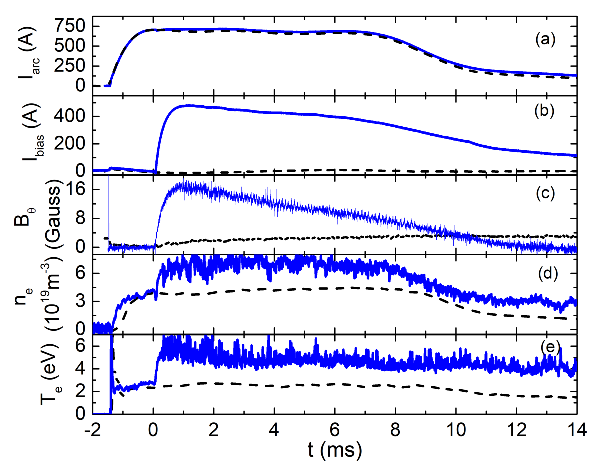

FIG. 3. Typical temporal evolution of a single argon plasma gun discharge in PHASMA. Solid blue traces are with bias current and black dashed lines are without bias current. (a) arc current; (b) bias current; (c) azimuthal magnetic field at $r = 2$ cm; (d) plasma density at $r = 0$ cm; (e) electron temperature at $r = 0$ cm.

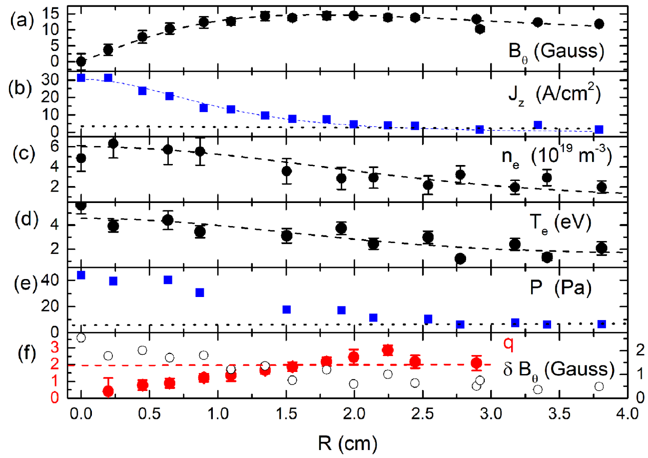

FIG. 4. Radial profile of a flux rope for $B_z = 375$ Gauss and $I_{bias} = 500$ A. (a) Azimuthal magnetic field B_θ (black circles) and a fit assuming a Bennett profile (dashed line); (b) Axial current density, J_z (c) plasma density, n_e; (d) electron temperature, T_e; (e) Plasma pressure $P \approx n_e T_e$; (f) Black circles are the amplitude of δB_θ fluctuations and the red circles are the safety factor, q. Kink instability threshold $q = 2$ is marked by the red dashed line.

III. IDENTIFICATION OF KINK INSTABILITY

A. Safety Factor, q, Profile

The measured magnetic field and pressure profiles are remarkably consistent with the classic Bennett profile for a z-pinch in magnetohydrodynamic (MHD) equilibrium; similar results were reported for flux ropes in the RSX device.[21] The azimuthal magnetic field profile is plotted in Fig. 4a, and is well fit with a Bennett profile of $B_\theta(r) = 2 \times 15 \frac{1.7 \times r}{1.7^2 + r^2}$ with a characteristic radius of 1.7 cm. The axial current density derived from the measured azimuthal magnetic field is $J_z = \frac{1}{\mu_0} \frac{1}{r} \frac{d}{dr}(r B_\theta)$ (see Fig. 4b). Figures 4c and 4d show the measured electron density and electron temperature profile for the flux rope. The resultant pressure profile is shown in Fig. 4e, where $P = n_e k_B T_e$ and k_B is the Boltzmann constant. The ion pressure is ignored assuming an ion temperature much smaller than the electron temperature. From fits of the J_z and P profiles, we determine the radius of the flux rope to be 2 cm; note the black dotted lines in the J_z and P profile plots represent the background levels for both quantities. The safety factor profile, $q(r) = \frac{4\pi^2 r^2 B_z}{\mu_0 L_0 I(r)}$, is plotted with red squares in Fig. 4f. Extending to the edge of the current channel, a radius of 2 cm, $q < 2$ is satisfied. Therefore, the entire non-line tied flux rope is vulnerable to the kink instability.[12] Indeed, the magnetic fluctuations δB_θ observed in PHASMA are distributed globally (see the open black circles in Fig. 4f). Globally distributed fluctuations with clear internal $m = 1$ mode structure were also observed in ReWM.[14] If $q < 2$ were to be satisfied in a restricted region of the flux rope, e.g., $r < R_0$, where R_0 is radius of flux rope, an internal kink mode would grow without significant perturbation of the plasma edge.[13] Here, the entire flux rope is unstable. The kink mode is therefore an external kink mode and significant perturbations at R_0 are observed.

The global nature of this kink instability is also evident in high-time-resolution visible light images of the flux rope. Images obtained with a fast camera using a sample rate of 75,000 frames/s are shown in Fig. 5. Figure 5a shows the temporal evolution of a slice of the plasma along the y axis at $z = -0.3$ m. Black and blue dashed lines show the amplitude of the image fluctuations at center and edge of the flux rope, respectively. The frequency of the fluctuations is consistent with those observed in δB_θ. The plasma edge is clearly undergoing significant perturbation. Comparing the displacement of flux rope edge at $z = -0.5$ m (Fig. 5b), to that at at $z = -0.3$, we observe a slight increase in the displacement closer to the bias plate. The increase in perturbation amplitude closer to the bias plate is consistent with a non-line tied boundary condition at the bias plate.

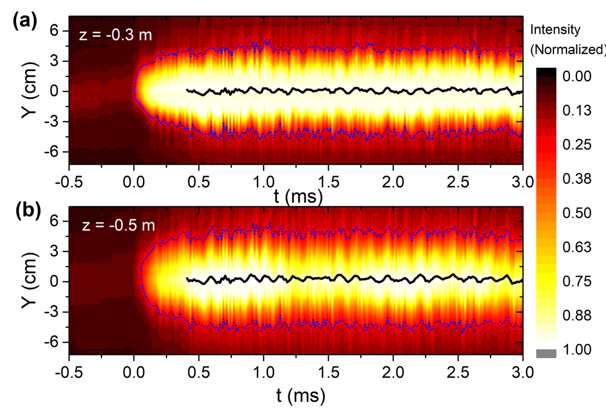

FIG. 5. Contour plots of visible emission light intensity during a flux rope discharge recorded at $z = -0.3$ m (a) and $z = -0.5$ m (b) with a fast camera operating at 75,000 frames/s. The black lines show the amplitude of the fluctuations at the center $Y = 0$ while the blue lines show the amplitude of the fluctuations in the outer region of the flux rope.

B. Helicity and Paramagnetism

For a flux rope with both B_θ and B_z, the equilibrium magnetic field has a specific helical pattern, right (left) handedness for $B_z \| J_z$ ($B_z \| -J_z$). Fluctuations with helical structure that matches the equilibrium magnetic field structure experience less twisting than those with the opposite helicity, i.e., less stabilizing magnetic tension force. Therefore, the helical perturbations that match the equilibrium structure are more vulnerable to the kink instability.[10] In other words, kink instabilities with $\vec{k} \cdot \vec{B} \approx 0$ should dominate.[9] For the experimental configuration shown in Fig. 2, $B_z \| J_z$, kink fluctuations with right handed helicity, $k_z \cdot m < 0$, should dominate.[21]

Figure 6a shows the temporal evolution of δB_θ fluctuations obtained with the azimuthally distributed magnetic probes (A

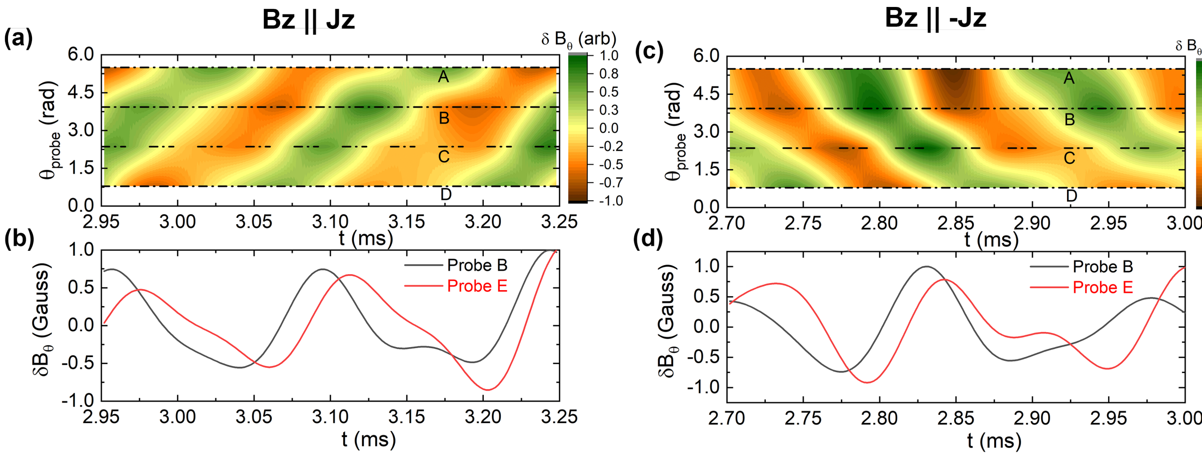

FIG. 6. Propagation of a coherent perturbation along the azimuthal and axial directions for two different experimental scenarios: background magnetic field B_z parallel and anti-parallel to J_z. Contour plots (a,c) of δB_θ fluctuations as measured with the four magnetic probes, A to D, demonstrate that the fluctuation propagates along $+\hat{e_\theta}$ when $B_z \| J_z$ and along $-\hat{e_\theta}$ when $B_z \| -J_z$. (b,d) show time series of δB_θ fluctuations obtained from axially spaced probes B and E, indicating $k_z < 0$ for both scenarios. Thus, the fluctuations exhibit right (left) hand helicity for $B_z \| J_z$ ($B_z \| -J_z$), consistent with a kink instability.

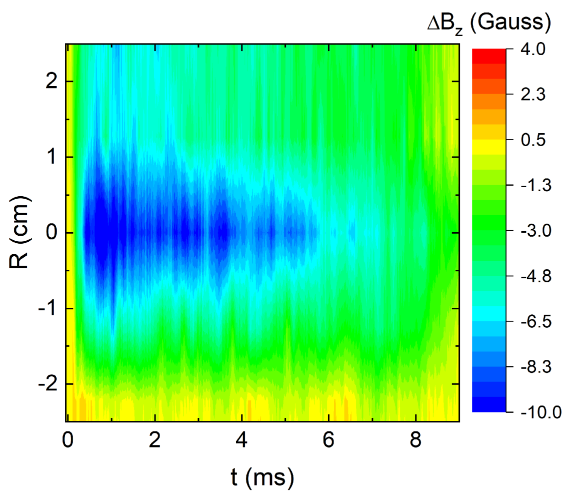

FIG. 7. The spatial-temporal evolution of the change in axial magnetic field, ΔB_z. The change of $\Delta B_z \sim -10$ Gauss results from the paramagnetic effect of the kink instability (5-6 Gauss) superimposed on the diamagnetic effect due to the radial pressure gradient (-14 Gauss).

to D) at the same radial location. A coherent large-amplitude mode is clearly progating in the azimuthal direction. From the measured phase difference, the azimuthal number m is determined. The frequency of the mode is ~ 7 kHz and propagates along $+\hat{e_\theta}$ with $m = +1$, the electron gyration direction. The phase difference between probes A and E located at similar θ, but different axial positions is shown in Fig. 6b, indicating that the mode propagates along $-\hat{e}_z$, from the plasma gun tip to the bias plate. This mode has right hand helicity, as expected for a kink instability. With the axial magnetic field reversed, $B_z \| -J_z$, as is shown in Fig. 6c, the mode helicity flips to left handed, with k_θ along the electron gyration direction and k_z pointing from the gun tip towards the bias plate (Fig. 6d), $m < 0$, $k_z < 0$.

One consequence of the right (left) handed helicity of the kink instability is its paramagnetic effect.[9,35] In laboratory experiments, proper accounting of contributions from other factors is also needed to reveal the paramagnetic effect of kink instability. For example, diamagnetic effects due to the plasma pressure gradient must be quantified and included in any analysis. For PHASMA, the expected decrease in axial magnetic field due to diamagnetic effects is given by $\Delta(n_e T_e) = -45$ Pa $= \Delta(B^2/2\mu_0) = B_z \Delta B_z/\mu_0$, $\Delta B_z = -14$ Gauss. As is shown in Fig. 7, the net change in axial magnetic field during the flux rope evolution is - 10 Gauss, meaning that the paramagnetic contribution from the kink instability is roughly 4 Gauss, close to estimated increase in axial magnetic field that should result from the azimuthal component of the bias current $\Delta B_z = \mu_0 I_{bias}/2R \cdot (B_\theta/B_z) = 5-6$ Gauss. For context, we note that for high-current operation in RWM, $\Delta(n_e T_e) = -350$ Pa led to a diamagnetic effect of $\Delta B_z = -70$ Gauss, while twisting of their 5 kA bias current introduced $\Delta B_z \sim 100$ Gauss. The overall paramagnetic effect was therefore $\Delta B_z \sim 30$ Gauss, close to their reported result.[14] Based on these measurements, the coherent fluctuation observed in PHASMA exhibits the expected paramagnetic feature of a kink instability.

C. Growth Rate

A kink instability is expected to grow on an MHD time scale, $\tau_A \sim 50\mu s$ in PHASMA.[15,36] Since τ_A is smaller than one oscillation of the observed m = 1 structure, we have focused our attention on the growth of the amplitude of the very first oscillation of B_θ. There are two contributions to B_θ in the initial phase of the flux rope formation. One contribution arises from the increasing bias current in the flux rope and the other comes from the increase (if any) in the amplitude of the $m = 1$ perturbation. Fig. 8a shows the experimentally measured B_θ (blue line) as a function of time. The black dashed line shows the calculated increase in B_θ at the fixed radial location, r, of the probe due to the axial plasma current. The difference between these two signals B_θ^{kink} results from the perturbation of the kink instability shifting the axis of the plasma current, dr/dt. $B_\theta^{kink} = \int dt I_{bias}(dr/dt)\frac{\mu_0}{2\pi R_P^2}$, where R_P is magnetic probe's initial radial location.

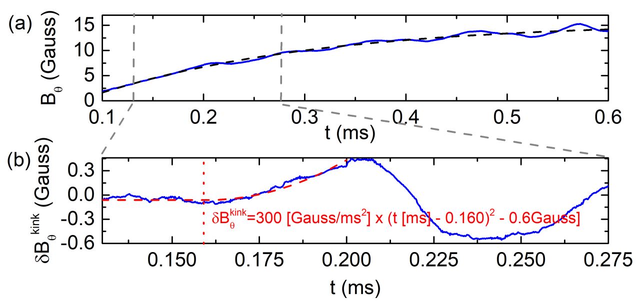

FIG. 8. (a) Measured B_θ (blue solid line) and the calculated B_θ based on the bias current (black dashed line) for the location of the magnetic probe; (b) Difference between measured and calculated B_θ (blue line) and the quadratic fit (red dashed line); The dotted vertical red line denotes the time at which the kink instability begins to grow.

The initial phase of the perturbation, shown with a dotted red quadratic fit line in Fig. 8b demonstrates that the first quarter of first oscillation of B_θ^{kink}, from $t = 0.160$ ms to $t = 0.183$ ms is not a sinusoidal wave, but a signal that is growing in time. Note that the bias current is 160 A when the kink instability starts to grow at t = 0.160 ms, completely consistent with a threshold value for $q = 2$. The bias current is growing linearly during this short period, at a rate of $dI_{bias}/dt = 1.2$ A/μs. Therefore, the quadratic nature of the growth implies that dr/dt is constant, i.e., the kink instability is growing linearly. Linear growth of the shift in r is independently verified with camera images, in which $dr/dt \approx 0.1$ mm/μs is observed. Using measured values, the predicted amplitude of the quadratic term in B_θ^{kink} is $\frac{1}{2}\frac{dI_{bias}}{dt}\frac{dr}{dt}\frac{\mu_0}{2\pi R_P^2} = 200$ Gauss/ms^2, comparable to the value of 300 Gauss/ms^2 obtained from the quadratic fit. Linear growth of a kink instability has also been reported in other experimental systems.[15,16]

IV. EVIDENCE FOR AN ALFVÉNIC MODE

The real frequency of a kink instability in the plasma frame is zero.[37] In the laboratory frame, observed finite frequencies are typically attributed to Doppler shifts introduced by either axial flow or $E \times B$ drift. The observed frequency of the kink instability reported here cannot be explained by $E \times B$ drift. The observed frequency versus axial magnetic field strength is shown in Fig. 9a. As is shown in Fig. 9b, the calculated $E \times B$ drift frequency $f_{E\times B} = E_r/B_z 2\pi R$ is one order larger than the observed frequency and decreases monotonically with increasing background axial magnetic field strength B_z. The radial electric field is derived from calculations of the plasma potential[38,39] based on the values of V_f and T_e as measured with the triple Langmuir probe, $E_r = d(V_f + 5.3 \times T_e)/dr$. According to measurements in RSX,[11,21] which operated with similar plasma parameters as used in this study, the Doppler shift from axial flow contributes to the observed frequency of the kink instability. Figure 9c shows the estimated Doppler shift due to axial flow,

$$f_{VZ} \approx \frac{V_z}{4L}\sqrt{1 - V_z^2/V_A^2} \cdot \frac{I_{bias}}{I_{KS}/2}, \qquad (1)$$

where the last term includes the contribution from a bias current larger than the threshold value[12,36] and axial flow speed is given by $V_z = 0.4c_s$, where c_s is ion sound speed. While comparable in magnitude to the observed frequencies, the scaling of f_{VZ} with increasing magnetic field is completely inconsistent with the observations. Thus, the discrepancy between f and f_{VZ} suggests the existence of another mode with finite real frequency.

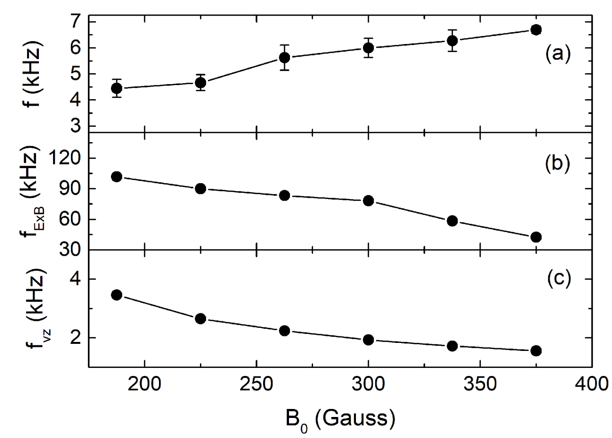

FIG. 9. (a) Observed frequency of coherent fluctuation as a function of applied axial magnetic field strength. (b) Estimated Doppler shifted frequency $f_{E\times B}$ that would result from $E \times B$ drift. (c) Estimated Doppler shift frequency f_{vz} that would result from axial flow V_z.

A. Fluctuation Frequency Spectra

The evolution of the frequency spectrum of the fluctuations δB_θ (Figure 10a) during the relatively long 10 ms discharges in PHASMA (compared to $\sim$ 1 ms in RSX) provides an opportunity to identify the wave mode at later times after the amplitude of the global kink instability decreases. We use the inductance of the flux rope as one indicator of amplitude of global kink instability. The global twisting (deformation) of a flux rope introduces extra inductance into the external bias current circuit. The bias circuit inductance is related to the

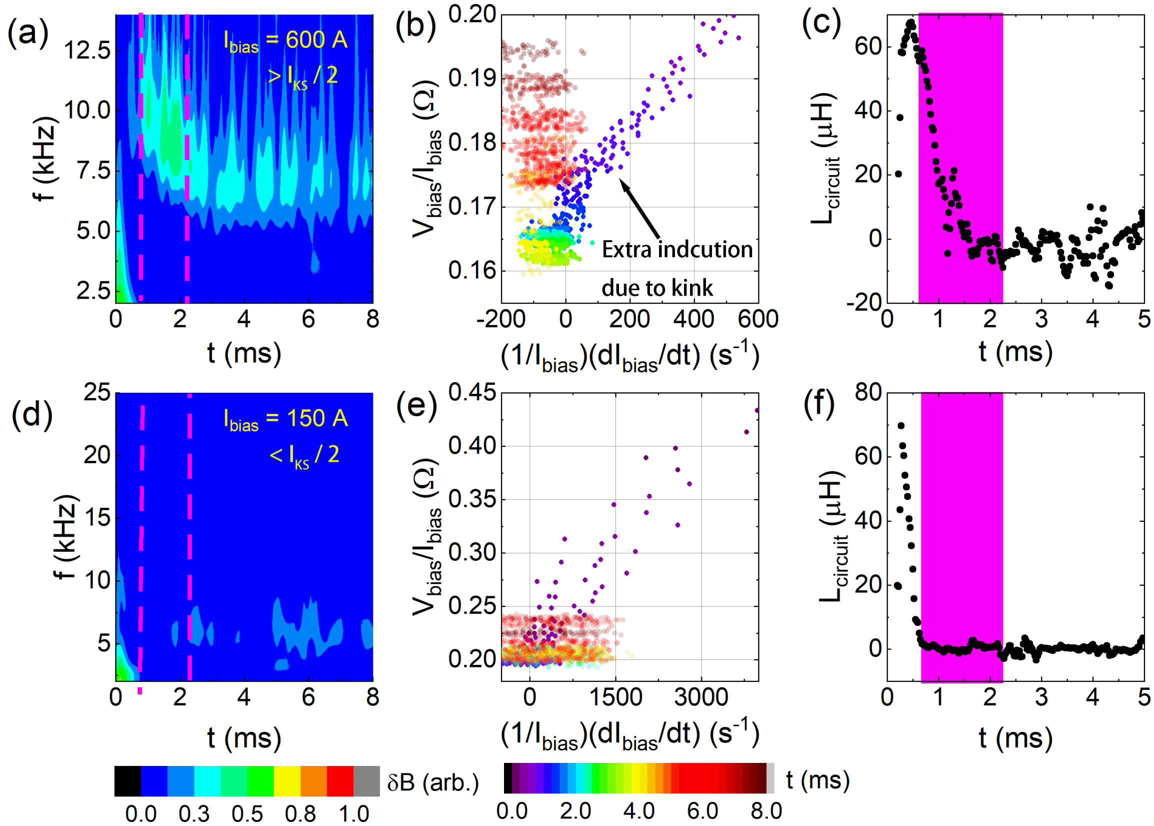

FIG. 10. (a) The frequency spectrum of δB_θ for $I_{bias} = 600$ A; (b) Temporal evolution of $I_{bias}(t)$ and $V_{bias}(t)$ in coordinates of $\frac{dI_{bias}}{dt}\frac{1}{I_{bias}}$ along the x axis and $\frac{V_{bias}}{I_{bias}}$ along the y axis. The colors indicate time time intervals during the discharge. The slope of these data equals the effective inductance $L_{circuit}$ in the bias circuit. (c) Temporal evolution of $L_{circuit}$. (d-f) Similar to (a-c), but for $I_{bias} = 150$ A.

circuit impedance by

$$\frac{V_{bias}}{I_{bias}} = L_{circuit}\frac{dI_{bias}}{dt}\frac{1}{I_{bias}} + R_{circuit}, \tag{2}$$

where $L_{circuit}$ and $R_{circuit}$ are the inductance and resistance in bias circuit. Based on Eq. 2, Fig. 10b shows $I_{bias}(t)$ and $V_{bias}(t)$ in coordinates of $\frac{dI_{bias}}{dt}\frac{1}{I_{bias}}$ along the x axis and $\frac{V_{bias}}{I_{bias}}$ along the y axis. Different colors identify different time intervals in the discharge. The slope of this plot is $L_{circuit}$ and is shown in Fig. 10c as a function of discharge time. The decrease in $L_{circuit}$ from $t = 0.5$ ms to 2 ms is a clear indication that the amplitude of the global kink instability is decreasing. For comparison, the time evolution of $L_{circuit}$ for $I_{bias} = 150$, i.e., for a discharge current below the kink instability threshold, $I_{KS}/2 = 180$ A, is shown in Fig. 10e and 10f. Below threshold, no additional inductance appears in the bias circuit from $t = 0.5$ ms to 2 ms. Thus, the measured inductance provides a crude indicator of the amplitude of the global kink instability in our experiment.

The evolution of the δB_θ frequency spectrum shown in Fig. 10a is obtained through a wavelet analysis of the fluctuations. As the amplitude of global kink instability decreases from $t = 0.5$ ms to 2 ms, both the amplitude and frequency of the fluctuations decrease. After $t = 2$ ms, the contribution from global kink instability to the observed fluctuation frequency is negligible since the global deformation of the flux rope, as indicated by the dramatically smaller inductance, has ceased. Note that there is no change in the fluctuation amplitude and frequency without excitation of the kink instability (Fig. 10d). The presence of very weak fluctuation, still discernible in Fig. 10d, implies that the observed wave modes are a pre-existing fundamental modes in the plasma and the kink instability simply provides more free energy to this mode. Note also that frequency and amplitude of the mode remains almost constant even after the bias current has dropped by roughly 30% from $t = 2$ ms to 8 ms - further evidence that this wave mode is not a global kink instability.

From t = [0.5 ms, 2 ms] to t = [2 ms, 8 ms], the frequency of the fluctuations decreases by ~ 2 kHz, consistent with the expected Doppler shift of a global kink instability arising from axial flow. The predicted value of $f_{VZ} = 1-2$ kHz, close to observed frequency, is consistent with Ryutov's model for non-lined tied kink instabilities in a flowing plasma.[12] While the kink instability only persists until $t = 2$ ms, 2 ms is still much longer than the Alfvén transit time, $\sim 40\tau_A$, and is comparable to the "long-lifetime" kink instabilities observed in RSX.[21] These PHASMA discharges last long enough that other plasma modes are readily identifiable.

B. Coupling to the Kink Instability

To investigate the relation between the kink instability and this new wave mode, we investigated the dependence of the amplitude of the mode on bias current from t = 2 ms to 8 ms, shown as blue circles in Fig. 11a. When $I_{bias} < 180$ A, the amplitude of the mode increases with increasing bias current, but the rate of increase is much smaller than for $I_{bias} > 180$ A. The predicted threshold current for the kink is $I_{KS}/2 \approx 180$ A. The amplitude of the global kink instability is also calculated by subtracting the amplitude of the additional mode from the total amplitude of fluctuations from t = 0.5 ms to 2 ms (red squares in Fig. 11a). The resultant amplitude of the kink instability is shown as black circles in Fig. 11b, verifying $I_{bias} = 180$ A is the threshold bias current for the global kink instability. Therefore, this additional large amplitude mode draws energy from the kink instability once it is excited.

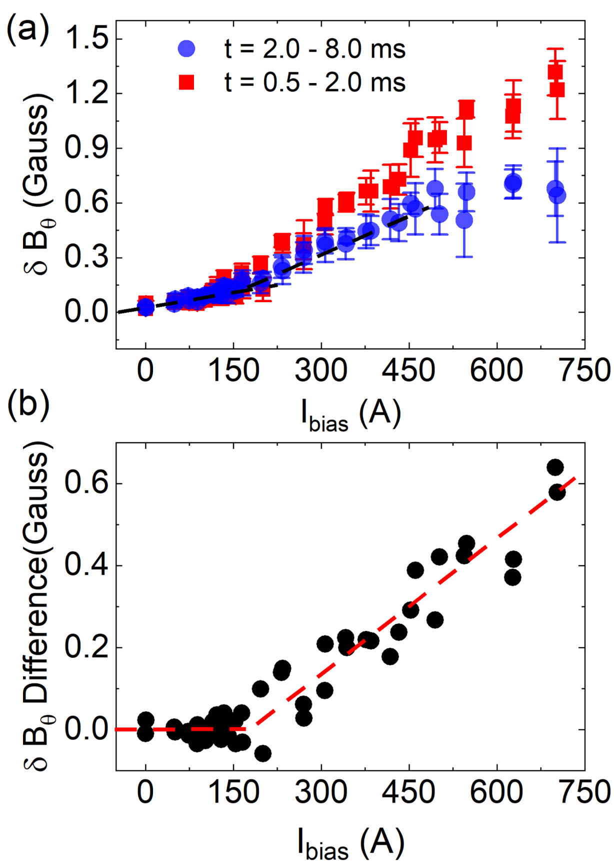

FIG. 11. (a) The dependence of amplitude of B_θ fluctuations from t = 2 ms to 8 ms (blue circles) and for t = 0.5 ms to 2 ms (red squares) as a function of bias current. (b) The dependence of global kink instability amplitude, deduced from the difference in the two amplitudes in (a) as a function of current.

C. Alfvénic Nature of the New Mode

The kink instability is just one branch of the Alfvén surface wave spectrum.[40] Thus, it seems reasonable that other Alfvénic wave modes could couple to and draw energy from the kink instability. Two features of this mode that point towards an Alfvénic nature are the mode's frequency being less than the ion gyrofrequency and the strong perpendicular magnetic field fluctuations, δB_θ.

Very low frequency Alfvénic waves in an ideal MHD plasma propagate along the background magnetic field at the Alfvén speed, V_A. In PHASMA, the wave frequency is comparable to the ion gyrofrequency, $0.1 f_{ci} < f_{AW} < f_{ci}$, thus finite frequency effects must be included in the wave dispersion relation

$$f_{AW} = \frac{1}{2\pi}\sqrt{\frac{1}{\frac{1}{(k_z \overline{V}_A)^2} + \frac{1}{(2\pi f_{ci})^2}}}\,, \tag{3}$$

where k_z is the parallel wavevector and $\overline{V}_A$ is the average Alfvén speed, $\sqrt{2}V_A$.[21,41] The phase angle difference between the axially separated magnetic probes B and E is obtained from a correlation analysis and used to calculate k_z. Figure 12a shows k_z a function of bias current; black squares for $B_z = 225$ Gauss and blue squares for $B_z = 375$ Gauss. The coherence found in the correlation analysis is large, > 0.9, only for large bias currents, so smaller bias current $I_{bias} < 300$ A are not included in these plots. The plasma density and electron temperatures measured with the triple Langmuir probe do not increase with bias current when $I_{bias} > 300$ A, consistent with the relatively constant values of k_z seen in Fig. 12a if the mode is Alfvénic. The corresponding frequency of this mode f_{AW} is shown in Fig. 12b. Similar to the results for k_z, the frequency remains almost constant with increasing bias current I_{bias}, but increases with increased background magnetic field B_z. The theoretical predictions of f_{AW} based on the Alfvén dispersion relation of Eq. 3 is shown in Fig. 12c as a function of B_z. The uncertainty in f_{AW} shown by magenta shading is due to an assumed 10% uncertainty in both k_z and n_e. The experimental measurements of f_{AW} are plotted as black and blue squares and are consistent with the Alfvén dispersion relation.

Interestingly, the dispersion relation also predicts the observed increase of f_{AW} with increasing B_z, a key feature which could not be explained by Doppler shift effects arising from axial flow or $E \times B$ drift. We note that other kink experiments have also reported an increase in the kink instability frequency with increasing B_z.[14,42] Fluctuations with somewhat similar characteristics were observed on the Encore Tokamak at similar plasma parameters. Those fluctuations were identified as drift Alfvén waves.[43] However, in PHASMA the coupling between drift waves and Alfvén waves is not expected to be significant because the expected parallel phase speed (60 km/s) of the drift wave is much larger than V_A.

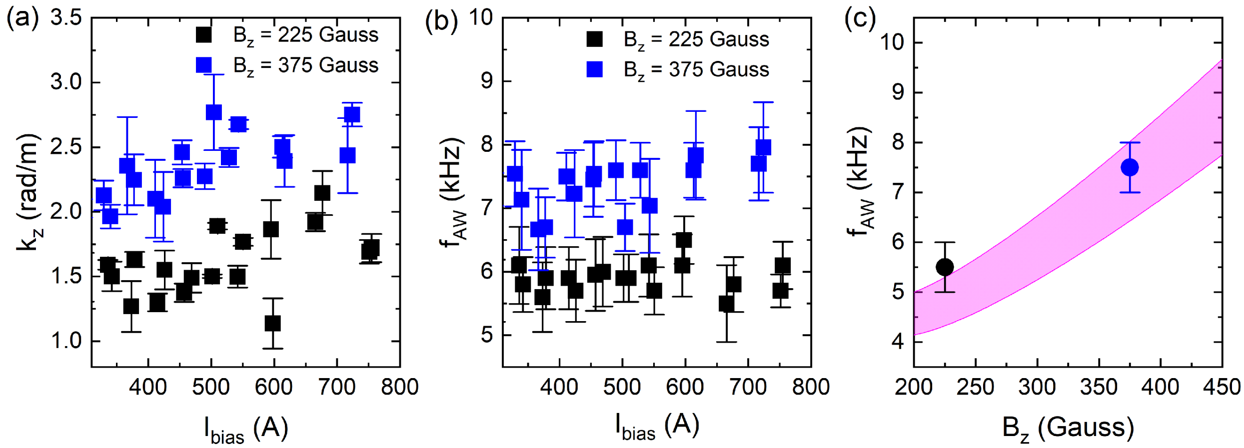

FIG. 12. (a) Parallel wavevector k_z and (b) wave frequency as a function of bias current for $B_z = 225$ Gauss (black squares) and 375 Gauss (blue squares). (c) Range of theoretical predictions for the Alfvén wave frequency f_{AW} as a function of background magnetic field B_z (shaded region) assuming 10% uncertainties in n_e and k_z. Black and blue circles are the measured values of f_{AW} for $B_z = 225$ Gauss and 375 Gauss.

D. Frequency Limit of the Mode

If the observed wave mode is Alfvénic nature, it should exhibit significant changes for frequencies near the ion cyclotron frequency. To determine if there is a frequency limit for this mode, we compare measurements in two working gasses, argon ($f_{ci}^{Ar} = 14$ kHz) and hydrogen ($f_{ci}^{H} = 560$ kHz). Figure 13 shows the dependence of f_{AW} and normalized mode frequency $\frac{f_{AW}}{f_{ci}}$ on the bias current (argon as black squares and hydrogen as blue squares). In contrast to a nearly constant f_{AW} in argon, f_{AW} in hydrogen increases monotonically with bias current. These observations are consistent with those in other kink experiments in which no limit in mode frequency was seen when the normalized mode frequency is small, e.g., $f_{AW} < 0.1 f_{ci}$ in hydrogen RSX plasmas.[11,14] Whether or not these observations point to resonance at $f \approx 0.5 f_{ci}$ is not yet clear.

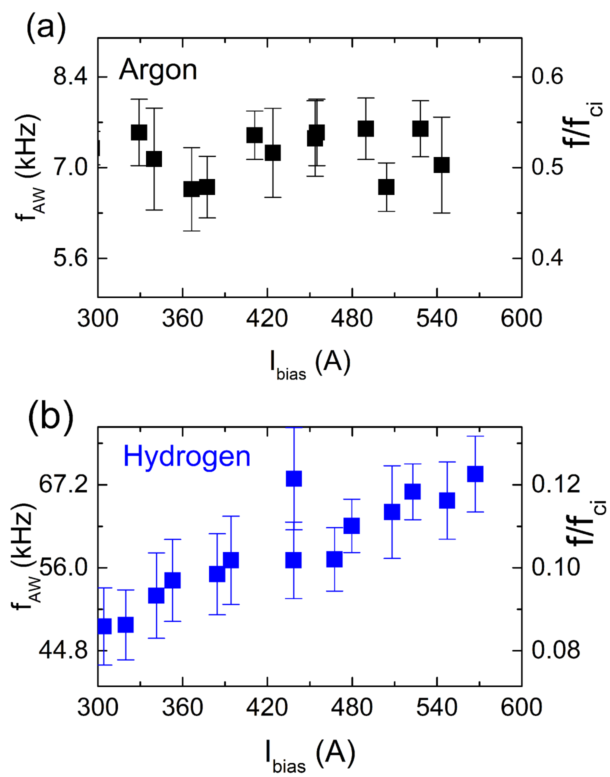

FIG. 13. The dependence of the mode frequency f_{AW} and the normalized mode frequency $\frac{f_{AW}}{f_{ci}}$ on bias current for (a) argon plasma and (b) hydrogen plasma. A frequency limit is observed in argon plasma when f_{AW} is a significant portion of f_{ci}.

V. CONCLUSION

In summary, a magnetic flux rope is successfully created with a pulsed plasma gun operating with argon gas in the PHASMA facility. A kink instability appears when the bias current exceeds $I_{KS}/2$, consistent with the prediction for the threshold current value for a non-line tied axial boundary condition. Both magnetic and visible light intensity fluctuation measurements indicate that the kink instability is globally unstable. From measurements of k_θ and k_z, the $m = 1$ fluctuations have right (left) handed helicity when $B_z \| J_z$ ($B_z \| -J_z$), exactly as predicted for a kink instability. The predicted paramagnetic effect of a kink instability is measured experimentally and the magnitude of the paramagnetism is consistent with predictions for a kink instability. Linear growth of the kink instability after onset is observed. However, the frequency of the observed fluctuations f is much larger than is explainable by a Doppler shift, f_{VZ}, due to axial flow. The differential frequency $f - f_{VZ}$ of the fluctations is attributed to another wave mode co-existing with kink instability. This wave mode is driven by the kink instability since the mode amplitude dependence on bias current tracks that of the kink instability. The new wave mode is consistent with an Alfvén wave dispersion relation. The frequency of the mode is constrained when it reaches a significant portion of f_{ci}. It is unclear if an Alfvénic resonance is occurring at $f \approx 0.5 f_{ci}$. In future studies, the ion temperature and bulk flow speed will be measured with LIF[44,45] to identify any possibly resonant interaction of the ions with the Alfvén wave that is coupled to the kink instability.

ACKNOWLEDGMENTS

We would like to express our deep appreciation to the late Dr. Thomas Intrator who constructed the original RSX device from which many of the components of PHASMA come. We also thank Dr. Glen Wurden of Los Alamos National Laboratory who helped with the transfer of the RSX components to the PHASMA laboratory. We thank the plasma physics group at the University of Wisconsin-Madison for the use of the plasma guns. This work is supported by NSF awards PHYS 1827325 and 1902111, NASA award 80NSSC19M0146, and DoE award DE-SC0020294.

DATA AVAILABILITY

The data that support the findings of this study are available from the corresponding authors upon reasonable requests.

[1] J. P. Freidberg, *Ideal Magnetohydrodynamics*, Cellular Organelles (Plenum Press, 1987).
[2] T. Sakurai, Publications of the Astronomical Society of Japan **28**, 177 (1976).
[3] R. Liu, B. Kliem, V. S. Titov, J. Chen, Y. Wang, H. Wang, C. Liu, Y. Xu, and T. Wiegelmann, The Astrophysical Journal **818**, 148 (2016).
[4] D. M. Rust and A. Kumar, The Astrophysical Journal **464**, L199 (1996).
[5] A. Vourlidas, Plasma Physics and Controlled Fusion **56**, 64001 (2014).
[6] M. Janvier, Journal of Plasma Physics **83**, 535830101 (2017).
[7] R. C. Jennison and M. K. Das Gupta, Nature **172**, 996 (1953).
[8] I. T. Chapman, Plasma Physics and Controlled Fusion **53**, 13001 (2010).
[9] S. C. Hsu and P. M. Bellan, Physical Review Letters **90**, 215002 (2003).
[10] M. Kruskal, J. L. Tuck, and S. Chandrasekhar, Proceedings of the Royal Society of London. Series A. Mathematical and Physical Sciences **245**, 222 (1958).
[11] I. Furno, T. P. Intrator, D. D. Ryutov, S. Abbate, T. Madziwa-Nussinov, A. Light, L. Dorf, and G. Lapenta, Physical Review Letters **97**, 015002 (2006).
[12] D. D. Ryutov, I. Furno, T. P. Intrator, S. Abbate, and T. Madziwa-Nussinov, Physics of Plasmas **13**, 032105 (2006).
[13] W. F. Bergerson, C. B. Forest, G. Fiksel, D. A. Hannum, R. Kendrick, J. S. Sarff, and S. Stambler, Physical Review Letters **96**, 15004 (2006).
[14] C. Paz-Soldan, M. I. Brookhart, A. J. Clinch, D. A. Hannum, and C. B. Forest, Physics of Plasmas **18**, 52114 (2011).
[15] A. L. Moser and P. M. Bellan, Nature **482**, 379 (2012).
[16] S. C. Hsu and P. M. Bellan, Physics of Plasmas **12**, 32103 (2005).
[17] I. Furno, T. Intrator, E. Torbert, C. Carey, M. D. Cash, J. K. Campbell, W. J. Fienup, C. A. Werley, G. A. Wurden, and G. Fiksel, Review of Scientific Instruments **74**, 2324 (2003).
[18] X. Sun, T. P. Intrator, L. Dorf, I. Furno, and G. Lapenta, Physical Review Letters **100**, 205004 (2008).
[19] X. Sun, T. P. Intrator, M. Liu, J. Sears, and T. Weber, Physics of Plasmas **20**, 112106 (2013).
[20] T. DeHaas, W. Gekelman, and B. Van Compernolle, Physics of Plasmas **22**, 82118 (2015).
[21] T. P. Intrator, I. Furno, D. D. Ryutov, G. Lapenta, L. Dorf, and X. Sun, Journal of Geophysical Research: Space Physics **112**, A05S90 (2007).
[22] R. F. Boivin and E. E. Scime, Review of Scientific Instruments **74**, 4352 (2003).
[23] E. E. Scime, J. Carr Jr., M. Galante, R. M. Magee, and R. Hardin, Physics of Plasmas **20**, 032103 (2013).
[24] R. S. Marshall, M. J. Flynn, and P. M. Bellan, Physics of Plasmas **25**, 112101 (2018).
[25] M. Hesse and P. A. Cassak, Journal of Geophysical Research: Space Physics **125**, e2018JA025935 (2020).
[26] C. B. Beatty, T. E. Steinberger, E. M. Aguirre, R. A. Beatty, K. G. Klein, J. W. McLaughlin, L. Neal, and E. E. Scime, Physics of Plasmas **27**, 122101 (2020).
[27] X. Zhang, E. Aguirre, D. S. Thompson, J. McKee, M. Henriquez, and E. E. Scime, Physics of Plasmas **25**, 23503 (2018).
[28] D. S. Thompson, R. Khaziev, M. Fortney-Henriquez, S. Keniley, E. E. Scime, and D. Curreli, Physics of Plasmas **27**, 73511 (2020).
[29] A. M. Keesee, E. E. Scime, and R. F. Boivin, Review of Scientific Instruments **75**, 4091 (2004).
[30] M. E. Galante, R. M. Magee, and E. E. Scime, Physics of Plasmas **21**, 055704 (2014).
[31] D. S. Thompson, T. E. Steinberger, A. M. Keesee, and E. E. Scime, Plasma Sources Science & Technology **27**, 065007 (2018).
[32] P. Shi, P. Srivastava, C. Beatty, R. S. Nirwan, E. E. Scime. (2020). *Incoherent Thomson Scattering System for PHASMA*. Manuscript submitted for publication.
[33] J. L. Kline, E. E. Scime, R. F. Boivin, A. M. Keesee, X. Sun, and V. S. Mikhailenko, Physical Review Letters **88**, 195002 (2002).
[34] I. A. Biloiu and E. E. Scime, Physics of Plasmas **17**, 113509 (2010).
[35] R. J. Bickerton, Proceedings of the Physical Society **72**, 618 (1958).
[36] I. Furno, T. P. Intrator, G. Lapenta, L. Dorf, S. Abbate, and D. D. Ryutov, Physics of Plasmas **14**, 022103 (2007).
[37] P. M. Bellan, Journal of Geophysical Research: Space Physics **125**, e2020JA028139 (2020).
[38] I. A. Biloiu and E. E. Scime, Physics of Plasmas **17**, 113508 (2010).
[39] X. Sun, A. M. Keesee, C. Biloiu, E. E. Scime, A. Meige, C. Charles, and R. W. Boswell, Physical Review Letters **95**, 25004 (2005).
[40] N. F. Cramer and I. J. Donnelly, Plasma Physics and Controlled Fusion **26**, 1285 (1984).
[41] V. M. Nakariakov, V. Pilipenko, B. Heilig, P. Jelínek, M. Karlický, D. Y. Klimushkin, D. Y. Kolotkov, D.-H. Lee, G. Nisticò, T. Van Doorsselaere, G. Verth, and I. V. Zimovets, Space Science Reviews **200**, 75 (2016).
[42] M. Zuin, R. Cavazzana, E. Martines, G. Serianni, V. Antoni, M. Bagatin, M. Andrenucci, F. Paganucci, and P. Rossetti, Physical Review Letters **92**, 225003 (2004).
[43] E. D. Fredrickson and P. M. Bellan, The Physics of Fluids **28**, 1866 (1985).
[44] C. Biloiu, X. Sun, E. Choueiri, F. Doss, E. Scime, J. Heard, R. Spektor, and D. Ventura, Plasma Sources Science & Technology **14**, 766 (2005).
[45] E. Scime, C. Biloiu, C. Compton, F. Doss, D. Venture, J. Heard, E. Choueiri, and R. Spektor, Review of Scientific Instruments **76**, 026107 (2005).